Heliyon 6 (2020) e03397

Contents lists available at ScienceDirect

Heliyon

journal homepage: www.cell.com/heliyon

Research article

Chrysotile asbestos treated with phosphoric acid as an adsorbent for ammonia nitrogen

Camila P. Girotto, Sílvia D. de Campos, Élvio A. de Campos *

Center for Engineering and Exact Sciences, Western Paraná State University – UNIOESTE, Rua da Faculdade, 645, Toledo, 85903-000, PR, Brazil

ARTICLE INFO

Keywords:
Chemical engineering
Materials chemistry
Brucite
Tridymite
$N–NH_3$
Magnesium pyrophosphate

ABSTRACT

The purpose of this study was to find an alternative application for chrysotile asbestos, given that there is a complete structure of extraction and production of this class of serpentine minerals, but its use is banned for many applications. The idea was to obtain a compound that could immobilize phosphate by triggering a reaction between the magnesium oxide and hydroxide contained in the mineral, without causing phosphate leaching. To this end, chrysotile ($Mg_3SiO_5(OH)_4$) was treated with phosphoric acid (H_3PO_4) in a molar ratio of 1:3 in an aqueous medium at 85 °C until the solvent evaporated, resulting in two different solid compounds, which were prepared in a similar manner. The first compound (cri/H_3PO_4 1:3)$_1$, was obtained by rinsing and then heat-treating it at 150 °C for 6 h, while the second one, (cri/H_3PO_4 1:3)$_2$, was rinsed after the heat treatment. Compound (cri/H_3PO_4 1:3)$_1$ underwent partial leaching, while compound (cri/H_3PO_4 1:3)$_2$ showed a mass increase of 48%, with the formation of crystalline magnesium pyrophosphate mixed with amorphous SiO_2. The latter compound adsorbed $N–NH_3$ at pH 10, following the pseudo-first-order model (activation energy = 8329 ± 1696 J mol^{-1}). Equilibrium experiments, which were performed following Hill's sigmoidal type S2 isotherm model, indicated that the adsorption phenomenon was governed by two processes, i.e., complexation up to the inflection point (K_H between 10.0 mg L^{-1} at 40 °C and 13.6 mg L^{-1} at 25 °C) followed by adsorption. The q_{max} varied from 18.0 to 19.6 mgN g^{-1} and the adsorbent was reusable, maintaining its initial adsorbent capacity during its first reuse. This material, which was tested on real effluents, presented a $N–NH_3$ removal rate similar to that shown by the test solutions. The treatment of chrysotile with H_3PO_4 conducts it to a composite that adsorbs ammoniacal nitrogen at pH 10 and it is reusable maintaining the adsorption capacity.

1. Introduction

Chrysotile asbestos, a serpentine mineral also known as white asbestos, is classified as a hydrous magnesium silicate. This mineral is formed as a result of metamorphic changes that occur in ultrabasic volcanic rocks (Anbalagan et al., 2010). Its structure consists of a tetrahedral layer of tridymite (SiO_4) covered by an octahedral layer of brucite ($Mg(OH)_2$), constituting a bilayer of brucite-tridymite whose chemical formula is $Mg_3SiO_5(OH)_4$ (Salinas et al., 2019). Chrysotile is a highly flexible and heat resistant fibrous mineral, which is why it is used to produce asbestos cement, textiles (Wang et al., 2014), papers, films (Liu et al., 2013), ceramics, thermal and acoustic insulation (Zaremba et al., 2010), catalysts and adsorbents (Petkowicz et al., 2008; Salinas et al., 2019; Jiang et al., 2019). However, inhaling chrysotile fibers causes respiratory illnesses such as asbestosis and lung cancer, so its use is regulated and even banned in some countries (Bernstein et al., 2018).

The chemical composition of chrysotile may cause it to interact with different acid or alkaline organic and inorganic compounds. When chrysotile reacts with alkaline compounds, these compounds interact with its tridymite layer, and when it reacts with acid compounds, they interact with its brucite layer (Teixeira et al., 2013; McCutcheon et al., 2015). Therefore, it is also used as feedstock for the production of silica, which is obtained after leaching the brucite layer with an acid solution. This silica, which has a large surface area, high porosity, and abundant acid sites, can be used an as an adsorbent in the production of zeolites and as a catalyst support (Valouma et al., 2016). Liu et al. (2007) produced and characterized amorphous silica nanowires made from acid-leached chrysotile. These nanowires were composed of $SiO_{1.8}.0.6H_2O$, and had a tetrahedral geometry and cylindrical morphology. Rozalen and Huertas (2013) compared chrysotile leached in nitric, sulfuric, and oxalic acid at room temperature (25 °C). The results of their FTIR and XRD analyses indicated that HNO_3 formed an amorphous siliceous material, H_2SO_4,

* Corresponding author.
E-mail address: elvioantonio@uol.com.br (É.A. de Campos).

https://doi.org/10.1016/j.heliyon.2020.e03397
Received 6 December 2019; Received in revised form 27 January 2020; Accepted 6 February 2020

which in turned formed amorphous silica that destroyed the brucite layer. On the other hand, oxalic acid induced the amorphization of chrysotile and the precipitation of $MgC_2O_4{\cdot}2H_2O$. Maletaškić et al. (2017) obtained silica nanofibers with a high surface area by applying the acid leaching method, using a solution of 1 mol L^{-1} of HCl.

As can be seen, a significant number of studies on chrysotile involve the treatment of this mineral with inorganic acid solutions to obtain silica by the acid leaching process. However, the brucite in chrysotile can also interact with acid compounds without the occurrence of leaching. One such possibility is by using phosphoric acid (H_3PO_4), a weak nonvolatile and nontoxic acid that differs from stronger acids such as HCl and HNO_3 (Gilani et al., 2018; Khoualdia et al., 2017). The structure of H_3PO_4 enables it to bind to other minerals containing magnesium and calcium (as in the case of chrysotile) due to the presence of phosphate (PO_4^{3-}), which cause these minerals to undergo surface modifications (Celerier et al., 2018). This interaction may result in different types of magnesium phosphate in compounds containing chrysotile silicate, such as $Mg_3(PO_4)_2$, $MgHPO_4$, $Mg(H_2PO_4)_2$, $Mg_2P_2O_7$, etc. (Mousa, 2010).

Acid-modified chrysotile can be employed to adsorb different types of contaminants in wastewater, such as ammonia, which is often present in rivers, water bodies and air (Ribas et al., 2014; Tu et al., 2019). This compound is found in ionized (NH_4^+) or non-ionized (NH_3) form, depending on the pH level. NH_3 is the more toxic of the two species, since it percolates through living cell membranes more easily than NH_4^+, causing ecological imbalance, increasing the breathing and heartbeat rates of aquatic organisms and impairing their liver and kidney functions (Soltani et al., 2015; Sugiyama et al., 2009). Human activities generate numerous types of polluting effluents containing high levels of ammonia, including the fertilizer, pharmaceutical, petrochemical and food industries, as well as solid wastes from pig and poultry farming and urban waste.

In this context, it is essential, on the one hand, to develop new applications for chrysotile asbestos, given the abundance of this mineral and the fact that the logistics for its exploration already exists, and on the other, to search for new alternatives for the treatment of wastewater containing ammonia. Therefore, this paper describes the results of reactions between chrysotile and phosphoric acid. The purpose of these reactions was to modify the structure of the mineral without leaching brucite and to use it as an adsorbent for the removal of ammonia from aqueous media.

2. Materials and methods

2.1. Materials and reagents

The adsorbents were synthesized using chrysotile asbestos donated by the Brazilian Chrysotile Institute (IBC), located in Goiânia, state of Goiás, Brazil and orthophosphoric acid 85% (NEON). Batch adsorption experiments were carried out using solutions prepared with NH_4Cl 99.9% (J.T. Baker). All experiments are conducted using distilled water.

2.2. Preparation of adsorbents

Chrysotile fibers were strained through 4 mm and 28 mm mesh sieves, and the portion retained on the sieves was rinsed with distilled water and oven-dried at 105 °C until its mass remained constant. The reactions were performed using a molar ratio of 1:3 of chrysotile to H_3PO_4, considering a molecular weight of 276 g mol^{-1} for chrysotile ($Mg_3Si_2O_5(OH)_4$) and 196 g mol^{-1} for phosphoric acid (H_3PO_4). Then, 50 mL of distilled water was added to the reactants and the mixture was heated to 85 °C until complete water evaporation. The experiments were then carried out using two procedures. In Method 1, the solid compound (cri/H_3PO_4 1:3)$_1$ was rinsed and then heat-treated at 150 °C for 6 h. In Method 2, the compound (cri/H_3PO_4 1:3)$_2$ was heat-treated at 150 °C for 6 h, rinsed in distilled water and oven-dried at 105 °C until it reached a constant mass.

The percent variation in mass of the material was determined by comparing it to the initial mass of chrysotile.

2.3. Analysis and characterization methods

The chrysotile and adsorbents were analyzed by differential scanning calorimetry (DSC) in a Shimadzu DSC-60 calorimeter, using 5 mg of each material. The calorimeter was heated from 30 to 500 °C at a heating rate of 10 °C min^{-1} and a synthetic air flow of 50 mL min^{-1} was applied.

The materials were also subjected to a thermogravimetric analysis (TGA) using a Perkin Elmer STA 6000 simultaneous thermal analyzer, which was heated from 30 to 600 °C applying a heating rate of 10 °C min^{-1} and a synthetic air flow of 50 mL min^{-1}.

An X-ray diffraction (XRD) analysis was performed using a Bruker D2 PHASER diffractometer equipped with a Cu tube, applying CuKα radiation (1.54184 Å), 30 kV voltage and 10 mA current. Diffractograms were recorded in the interval of 2Θ between 5 and 60°, with a variation of 0.050° s^{-1}.

The morphology was analyzed by scanning electron microscopy/energy dispersive X-ray spectroscopy (SEM/EDS). Chrysotile and adsorbent samples were spread on a double sided carbon tape, dried, and then coated with a thin layer of gold. Micrographs were recorded at different magnifications in AN SE module. EDS spectra were obtained using an Oxford Instruments PentaFET Precision probe.

A texture analysis was performed via N_2 physisorption to determine specific surface area, pore volume and average pore diameter in a Quantachrome Nova 1000 surface area analyzer, using the BET method. For this analysis, the material was oven-dried at 110 °C, and then dried with ultrapure nitrogen for 3 h in the analyzer.

Infrared spectra were recorded using the diffuse reflectance technique within the range of 4000 and 400 cm^{-1}, with resolution set to 0.5 cm^{-1}. The samples were pelleted with KBr, and the analyses were performed using a Perkin Elmer 1600 FTIR spectrophotometer.

The chemical stability of the (cri/H_3PO_4 1:3)$_2$ was inferred by the eventual release of magnesium ions during the adsorption tests. Magnesium concentration was determined in a Varian spectrophotometer SpectrAA 20 Gemini, using air/acetylene flame under gases flows of 8 mL min^{-1} and 9 mL min^{-1}, respectivelly. The analysis parameters were: wavelength of 2852 Å, slit 3mm and lamp current of 15 mA.

2.4. Batch adsorption tests

Ammonia nitrogen concentrations in the batch adsorption tests were determined by the phenate method (APHA, 2005). This was done by adding the following solutions to an aliquot of 50 mL of the ammonium solution: two drops of sodium tartrate, 2 drops of phenolphthalein, 1 mL of NaOH (6 mol L^{-1}), 3 mL of phenate, 1 mL of sodium hypochlorite (20%), and 0.5 mL of sodium nitroprusside. After 45 min of reaction, absorbance readings were taken at 635 nm with a Shimadzu UV-1800 UV/Visible scanning spectrophotometer.

The batch adsorption tests served to determine which of the two adsorbents was efficient, ((cri/H_3PO_4 1:3)$_1$ or (cri/H_3PO_4 1:3)$_2$), both at pH 10, with an adsorbent concentration of 10 g L^{-1}, initial ammonia nitrogen concentration of 50 mg L^{-1}, rotation speed of 170 rpm in a temperature controlled orbital shaking incubator at 30 °C (Marconi MA-420). Using the more efficient adsorbent, the effects of pH and temperature were evaluated in kinetic assays, and the adsorption isotherms and thermodynamic parameters were determined in equilibrium assays. The capacity of the more efficient adsorbent was also tested by treating a sample of effluent from a wastewater treatment plant (WTP) for subsequent reuse.

2.4.1. Kinetic tests

The behavior of the N–NH_3 adsorption process was evaluated as a function of pH and temperature at an initial concentration of 50 mg L^{-1} and adsorbent concentration of 10 g L^{-1}. During the experiments,

aliquots were collected and placed in individual flasks at time intervals of 0–240 min. When taking the aliquots, 2 mL of solution was removed from the system to analyze its N–NH_3 concentration. It was then centrifuged at 6000 rpm for 5 min, and 1 mL was removed and diluted in 50 mL of distilled water. The samples were analyzed by the phenate method. All the experiments were performed in triplicate in an orbital shaking incubator operating at a rotation speed of 170 rpm and controlled temperature. The adsorption equilibrium time was also determined.

2.4.1.1. Effect of pH. The effect of the pH level was evaluated by varying this parameter at alkaline levels of pH 8, 9, 10, 11, and 12, following the methodology described by Sugiyama et al. (2009). The tests were carried out at 30 °C under the same conditions described earlier herein.

2.4.1.2. Effect of temperature. Based on the best pH value, an evaluation was made of the effect of temperature on the adsorption tests performed in duplicate. The temperatures applied were 25, 30, and 40 °C. The pseudo-first-order (Eq. (2)) (Lagergren, 1898) and pseudo-second-order (Eq. (3)) (Ho et al., 1996) kinetic models were applied to the experimental data, and the adsorption rate constants (k_1 and k_2), pre-exponential factor (A), and activation energy (E_a) were determined according to the Arrhenius Eq. (4) (Fogler, 2006), using Origin software by the least squares method.

$$q_t = \frac{(C_i - C_t).V}{m} \tag{1}$$

In Eq. (1), q_t is the adsorption capacity at a time t (mg g^{-1}), C_i is the initial concentration of adsorbate in the liquid phase (mg L^{-1}), C_t is the concentration of adsorbate at a time t in the liquid phase (mg L^{-1}), m is the mass of adsorbent (g), and V is the volume of the solution (L).

$$q_t = q_e\left(1 - e^{-k_1 t}\right) \tag{2}$$

In Eq. (2), q_e is the equilibrium adsorption capacity (mg g^{-1}), k_1 is the pseudo-first-order adsorption rate constant (min^{-1}), and t is the adsorbate/adsorbent contact time (min).

$$q_t = \frac{k_2 q_e^2\, t}{1 + k_2 q_e\, t} \tag{3}$$

In Eq. (3), k_2 is the pseudo-second-order adsorption rate constant (g $mg^{-1} min^{-1}$).

$$k = Ae^{-\frac{E_a}{RT}} \tag{4}$$

In Eq. (4), k is adsorption rate constant, A is the pre-exponential factor, E_a is the activation energy (J mol^{-1}), T is the temperature (K), and R is the gas constant (J mol^{-1} K^{-1}).

2.4.2. Equilibrium experiments

2.4.2.1. Isotherms. Adsorption isotherms were created by varying the initial concentration of N–NH_3 from 10 to 250 mg L^{-1} and employing the best timing and pH conditions at 25, 30, and 40 °C, using a concentration of 10 g L^{-1} of adsorbent. All the experiments were performed in duplicate. The amount of N–NH_3 adsorbed by the solid was determined according to Eq. (1).

The q_e vs. C_e graph was plotted based on the data obtained. The experimental data were then fitted to the Langmuir sigmoidal (Eq. (5)) and Hill sigmoidal (Eq. (6)) models, determining the adsorption constants for each model (K_L, q_{max}, K_S, K_H, and m) (Limousin et al., 2007).

$$q_e = \frac{q_{max}\, K_L\, C_e}{1 + K_L C_e + \frac{K_s}{C_e}} \tag{5}$$

In Eq. (5), q_e is the quantity of adsorbate per unit of adsorbent at equilibrium (mg g^{-1}), C_e is the adsorbate equilibrium concentration (mg L^{-1}), K_L is the Langmuir adsorption equilibrium constant (L mg^{-1}), and K_s is the sigmoidal adsorption equilibrium constant (mg L^{-1}).

$$q_e = q_{max}\frac{C_e^m}{K_H^m + C_e^m} \tag{6}$$

In Eq. (6), q_{max} is the maximum adsorption capacity (mg g^{-1}), C_e is the adsorbate equilibrium concentration (mg L^{-1}), K_H is the equilibrium constant (mg L^{-1}), and m is a parameter of Hill's sigmoidal model.

2.4.3. Reuse of the adsorbent

2.4.3.1. Recovery. After performing the adsorption tests at an initial concentration of 250 mg L^{-1} of N–NH_3 (the highest tested concentration), the solution was filtered, and the adsorbent was rinsed with distilled water and heat-treated at 150 °C for 6 h (DCS analysis). The solid was characterized based on mass, TGA, XRD, and FTIR analyses to detect changes in its structure after the adsorption process.

2.4.3.2. Adsorption tests. A batch adsorption test was carried out using a synthetic solution of ammonium (250 mg L^{-1}) and the recovered adsorbent, employing the best condition determined previously (pH and temperature) in order to evaluate the adsorption capacity of the adsorbent after its first use.

2.4.4. Adsorption test on a sample of treated wastewater

In addition to the adsorption tests the (cri/H_3PO_4 1:3)$_2$ was also tested on a sample of effluent, that was provided by the wastewater treatment plant (WTP) of the company SANEPAR, located in the city of Umuarama, in northwestern Paraná, Brazil.

The effluent sample was characterized to determine its pH, color, turbidity, chemical oxygen demand (COD) and ammonia nitrogen (N–NH_3) concentration, using the APHA method (2005). The concentration of calcium, magnesium and iron ions was determined by total reflection X-ray fluorescence (TXRF), using a spectrometer S2 PICOFOX (Bruker AXS Microanalysis GmbH) according the methodology described by Espinoza-Quiñones et al. (2015). Briefly, 10 μL of gallium standard solution (1,0 g L^{-1}, Sigma) and 100-μL of polyvinyl alcohol were added to 890 μL of the effluent sample to obtain a gallium concentration of 10 mg L^{-1} as internal standard. Then, 10 μL of this solution was careful deposited over a quartz disc (30 mm in diameter and 3 mm thickness) and left to dry at 25 °C in a laminar flow hood. The excitation source was a Mo target operating at 50 kV, 602 μA and excitation time of 1000 s.

3. Results and discussion

3.1. Characterization of the adsorbents

Two distinct solid compounds, (cri/H_3PO_4 1:3)$_1$ and (cri/H_3PO_4 1:3)$_2$, were produced by the reaction between chrysotile and phosphoric acid. The first compound, (cri/H_3PO_4 1:3)$_1$, was the product of the reaction between chrysotile and phosphoric acid rinsed immediately after the reaction. The compound (cri/H_3PO_4 1:3)$_2$ was obtained by heat-treating it at 150 °C for 6 h after the acid treatment, then rinsing and drying it at 105 °C until it reached a constant mass. The data in Table 1 show the mass variations that occurred as a function of the different preparation methods.

In Table 1, note that compound (cri/H_3PO_4 1:3)$_2$ showed an increase in mass compared to its initial value. In contrast, the mass of compound (cri/H_3PO_4 1:3)$_1$ showed practically no variation at the end of the preparation process. However, although the same quantities of chrysotile and phosphoric acid were used in both preparation methods, leaching was found to occur when rinsing with water before the heat treatment at 150 °C for 6 h (Method 1). After the heat treatment, both compounds showed a minor mass loss, although that of (cri/H_3PO_4 1:3)$_2$ was greater.

Table 1. Mass variations resulting from the reactions employed to obtain the solid compounds (cri/H_3PO_4 1:3)$_1$ and (cri/H_3PO_4 1:3)$_2$.

Solid compound	Chrysotile mass (g)	H_3PO_4 mass (g)	Mass before heat treatment (g)	Mass after heat treatment (g)
(cri/H_3PO_4 1:3)$_1$	2.49	3.45	2.56	2.46
(cri/H_3PO_4 1:3)$_2$	2.49	3.45	3.73	3.68

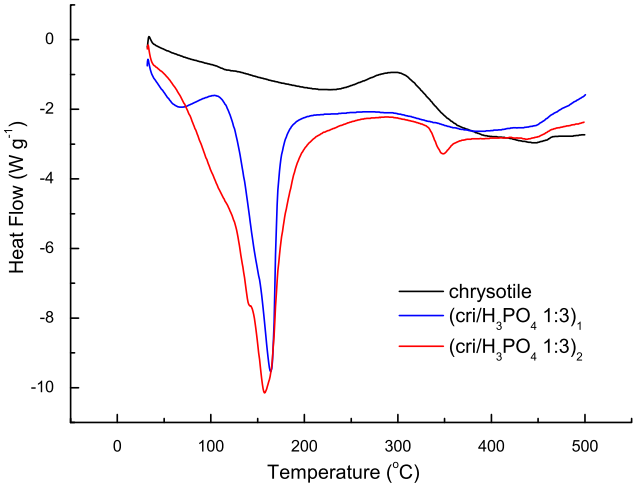

Figure 1. DSC curves of pure chrysotile and the compounds (cri/H_3PO_4 1:3)$_1$ and (cri/H_3PO_4 1:3)$_2$.

This indicates that the chrysotile/H_3PO_4 compounds were modified by the heat treatment, immobilizing the phosphates in the solid structure and thereby preventing them from dissolving during rinsing. To evaluate the changes that occurred in the chrysotile structure, the chrysotile and the two compounds were analyzed by DSC and TGA. Figures 1 and 2, respectively, illustrate the results of these analyses.

In Figure 1, note the modifications in the DSC curves of the compounds (cri/H_3PO_4 1:3)$_1$ and (cri/H_3PO_4 1:3)$_2$ when compared to that of the pure chrysotile, which showed no crystallization peak or phase change up to 500 °C. The broad exothermic peak at approximately 300 °C, which is not found in all chrysotile minerals (Wypych et al., 2004), is probably due to the thermal decomposition of some carbonates contained in this mineral species (Kusiorowskie et al., 2012).

The two compounds also showed no crystallization peak or change in their crystalline phase up to 500 °C. Moreover, the peak attributed to the thermal decomposition of carbonates was also absent, given that they decompose in acid media. Both compounds showed endothermic peaks between 100 and 200 °C, the most intense one occurring at 150 °C, which is close to the boiling point of H_3PO_4 (158 °C). The compounds were therefore heat-treated at 150 °C. The compound (cri/H_3PO_4 1:3)$_2$ showed a less intense endothermic peak at around 350 °C, but this was not investigated since it was well above the temperature chosen for the heat treatment.

The thermogravimetric analysis (Figure 2) indicated that, unlike the two compounds, the pure chrysotile underwent a mass loss of approximately 5% when heat-treated up to 600 °C. This mass variation was attributed to the loss of adsorbed and absorbed water molecules (Wypych et al., 2004), and also to the decomposition of carbonates (Kusiorowskie et al., 2012).

Before the compounds were heat-treated at 150 °C (see Figure 2a), they presented three different regions of mass loss. The first one, which occurred up to 100 °C, corresponded to the loss of weakly bonded water molecules. This mass loss was greater in the compounds than in the pure chrysotile. Moreover, the mass loss of compound (cri/H_3PO_4 1:3)$_2$ was approximately 3-fold greater than that of compound (cri/H_3PO_4 1:3)$_1$. The second mass loss occurred at 150 °C and corresponded to about 7% in the case of (cri/H_3PO_4 1:3)$_1$ and 15% in that of (cri/H_3PO_4 1:3)$_2$. The third mass loss occurred in the region between 200 and 600 °C, where both compounds underwent a continuous mass loss, with (cri/H_3PO_4 1:3)$_1$ and (cri/H_3PO_4 1:3)$_2$ showing a final mass of 87% and 70%, respectively, compared to their initial mass. The third mass loss was

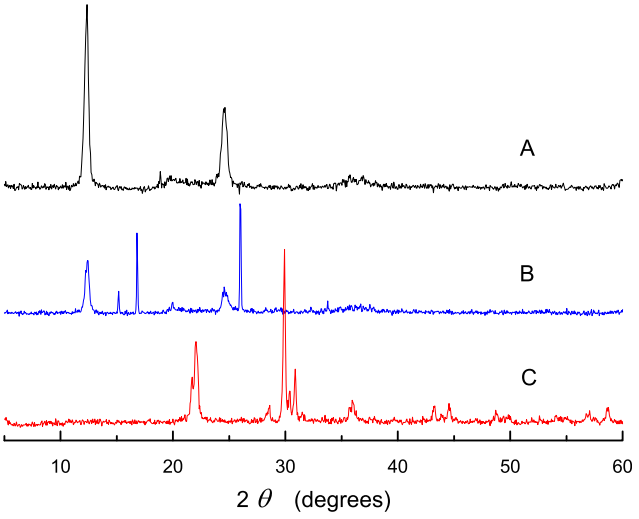

Figure 3. XRD patterns of: (A) chrysotile, (B) chrysotile treated with H_3PO_4 (cri/H_3PO_4 1:3)$_2$ before calcination, and (C) (cri/H_3PO_4 1:3)$_2$ after calcination.

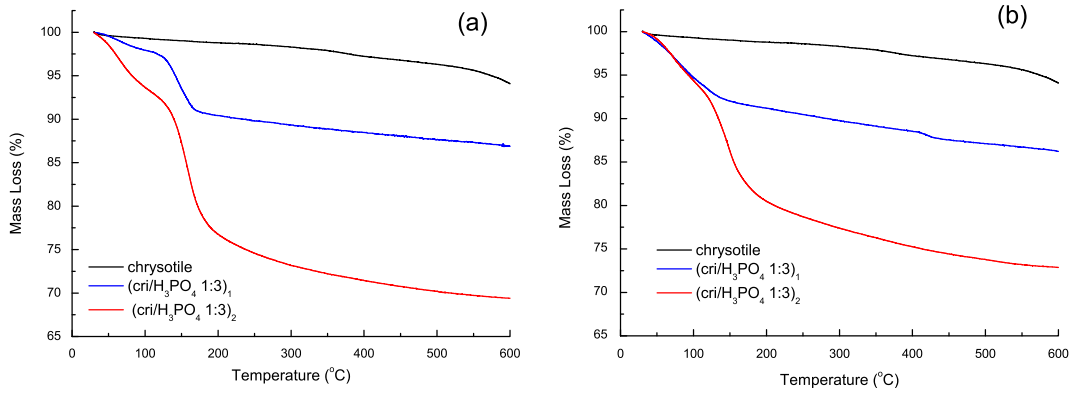

Figure 2. Thermogravimetric analysis of compounds (cri/H_3PO_4 1:3)$_1$ (cri/H_3PO_4 1:3)$_2$ (a) before and (b) after heat treatment at 150 °C for 6 h.

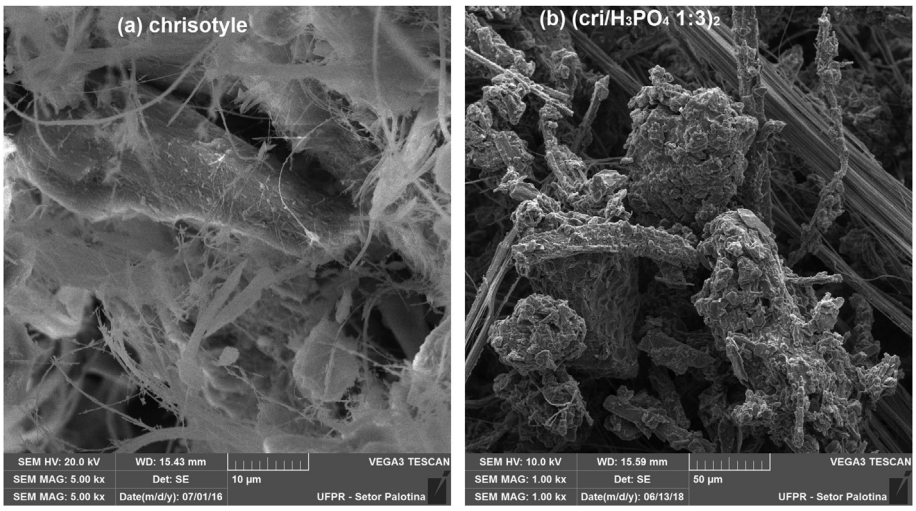

Figure 4. Micrographs of: (a) chrysotile fibers under 5000x magnification, and (b) (cri/H_3PO_4 1:3)$_2$ under 1000x magnification.

attributed to the condensation of chemically bonded hydroxyl groups and water molecules (Wypych et al., 2004), probably the ones that make up the silica contained in the structure.

The thermogravimetric analysis of compound (cri/H_3PO_4 1:3)$_2$ heat-treated at 150 °C for 6 h (see Figure 2b) showed almost the same profile as that prior to the treatment, except for the slight difference in the mass percentage remaining at 600 °C. The compound's total mass loss was lower when it was previously heated. On the other hand, compound (cri/H_3PO_4 1:3)$_1$ did not undergo a second mass loss at 150 °C, although the mass remaining after the thermogravimetric analysis was almost the same as that verified without heating.

The region where the second mass loss occurred may be attributed to the loss of strongly bonded water molecules, probably pertaining to phosphate groups immobilized within the structure of the resulting compound. This fact indicates that the product of the reaction between chrysotile and phosphoric acid requires heat treatment to stabilize it, given that no prior heating favors phosphate leaching and precludes the presence of strongly bonded water molecules in the structure of the final compound.

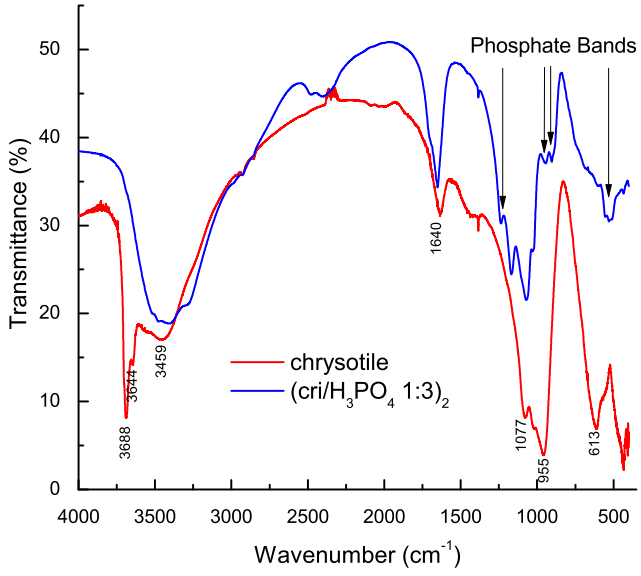

Figure 5. Infrared spectra of chrysotile and (cri/H_3PO_4 1:3)$_2$ recorded in the region of 4000 to 400 cm^{-1}.

In view of the fact that the more favorable preparation method is the one that results in greater mass gain, the analyses (mass, DSC, and TGA) indicated that the second method produced a more efficient reaction between chrysotile and phosphoric acid, resulting in a compound with a higher mass gain (with almost no leaching after rinsing) and producing greater modifications in the chrysotile structure. In the ammonia adsorption test at pH 10, compound (cri/H_3PO_4 1:3)$_1$ removed 41.2% of NH_3, while compound (cri/H_3PO_4 1:3)$_2$, removed 84.6%, as described in section 2.4, above. This indicates that Method 2 was also more efficient in the production of an adsorbent for ammonia nitrogen. Therefore, the XRD, SEM, and texture analysis by N_2 physisorption focused on the pure chrysotile and the compound obtained through the second method (cri/H_3PO_4 1:3)$_2$.

The XRD analysis (see Figure 3) indicates that the chrysotile presented a set of peaks at 12, 20, 25, and 37°, which are typical of the brucite and tridymite crystalline phases contained in the structure (Nakagaki et al., 2006; Anbalagan et al., 2010). The diffractogram of compound (cri/H_3PO_4 1:3)$_2$ in Figure 3b, which was recorded before the heat treatment at 150 °C, shows peaks at 15°, 17°, 26°, and 34° in addition to the peaks corresponding to the chrysotile phase, whose intensity was relatively lower than that of the pure chrysotile. These peaks are present, together with less intense ones, in the diffractogram of $Mg_3(PO_4)_2.22H_2O$ (Mousa, 2010). However, a search in the JCPDS database using Match software revealed that this set of peaks may also pertain to $Mg_{48}O_{147}Si_{34}$, corresponding to the mineral antigorite-T, whose structure does not contain phosphates. This might be the case were $Mg_3(PO_4)_2.22H_2O$ not crystalline. Hence, compound (cri/H_3PO_4 1:3)$_2$ may have contained both $Mg_{48}O_{147}Si_{34}$ and $Mg_3(PO_4)_2.22H_2O$ in its structure before it was heat-treated.

In Figure 3c, the diffractogram of compound (cri/H_3PO_4 1:3)$_2$ recorded after the heat treatment shows no chrysotile peaks or hydrous phases of magnesium phosphate and antigorite-T. However, several peaks are visible that coincide with those of magnesium pyrophosphate $Mg_2P_2O_7$ (Mousa, 2010; Aramendía et al. 1998). Aramendía et al. (1998) reported that the formation of this crystalline phase was only visible above 350 °C, but in our study, magnesium pyrophosphate was formed after heat treatment at 150 °C for 6 h. The remaining chrysotile silica was probably amorphous, since no peaks corresponding to any SiO_2 crystalline phase were visible.

The chrysotile structure depicted in Figure 4a was fibrous, as has been reported by several authors, including Rinaudo et al. (2003) and Wypych et al. (2005). After the reaction with phosphoric acid (see Figure 4b), the structure was less fibrous, although fibers mixed into a compact material were still visible. Similarly to the reaction with other mineral acids

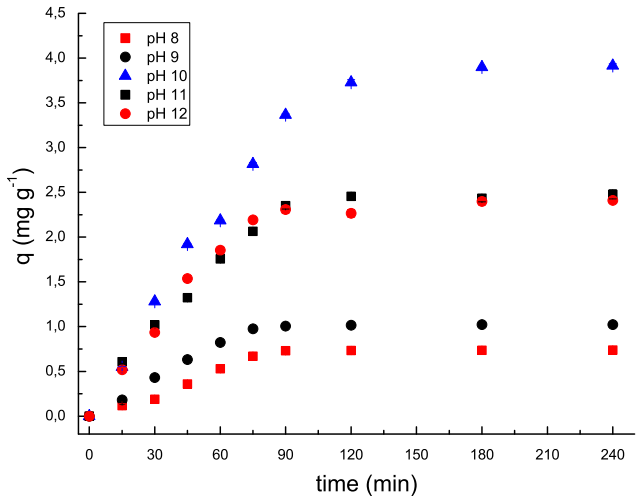

Figure 6. Amount of N–NH_3 adsorbed (mg g^{-1}) as a function of contact time at different pH levels. The initial concentration of N–NH_3 was 50 mg L^{-1}, that of the adsorbent was 10 g L^{-1}, rotation speed was 170 rpm, and temperature was 30 °C.

(Wypych et al., 2005), the reaction with H_3PO_4 may cause chrysotile to lose its octahedral layer with Mg^{2+} ions, resulting in the formation of an amorphous solid with a composition similar to that of silica with the same initial fibrous structure of chrysotile. This amorphous solid was mixed with a compact solid of irregular shape consisting of small fragments of amorphous silica fibers mixed with magnesium phosphates. An analysis of the EDX image revealed the presence of phosphorous in (cri/H_3PO_4 1:3)$_2$, which was absent from the chrysotile structure.

In Figure 5, the infrared spectra of chrysotile and (cri/H_3PO_4 1:3)$_2$ show bands at 3688 and 3644 cm^{-1} corresponding to OH stretching of internal and surface Mg–OH bonds, respectively, which constitute the brucite layers (Mendelovici et al., 2001). The bands at 3459 and 1640 cm^{-1} are associated with water molecules absorbed or adsorbed on chrysotile fibers (Wypych et al., 2004). The bands at 1077 and 955 cm^{-1} were attributed to the symmetric stretching vibration of Si–O–Si and Si–O bonds of the mineral's tridymite layer, while the band at 613 cm^{-1} is attributed to the internal vibration of the Mg–O bond (Wypych et al., 2005; Valouma et al., 2016). In the infrared spectrum of (cri/H_3PO_4 1:3)$_2$, note the absence of the bands of the brucite layer, and the presence of an intense broad band between 3600 and 3200 cm^{-1}. The intensity of the band corresponding to the water molecule at 1640 cm^{-1} is high, while that of the bands pertaining to the Si–O–Si and Si–O stretching vibrational mode is low compared to the chrysotile spectrum. This confirms that the brucite layer was destroyed and that a large volume of water molecules is contained in the structure of the solid compound. Also note the bands between 900 and 1200 cm^{-1} corresponding to the asymmetric stretching of P–O bonds of different types of phosphates, as well as the presence of a band close to 530 cm^{-1}, which corresponds to scissoring vibrations of O–P–O bonds of phosphates (Jastrzebski et al., 2011).

The N_2 physisorption analysis of the surface area and pore structure indicated that the treatment with acid reduced the compound's surface area. While the specific surface area of chrysotile was 14.7 m^2 g^{-1}, that of compound (cri/H_3PO_4 1:3)$_2$ was 3.2 m^2 g^{-1}, with a total pore volume of 7.1 × 10^{-3} cm^3 g^{-1} and an average pore diameter of 0.44 Å. This decrease in surface area and low porosity were probably due to the fact that the magnesium pyrophosphate in (cri/H_3PO_4 1:3)$_2$ was distributed throughout the voids in the fibrous structure of the amorphous silica remaining after the acid treatment, in microcrystalline form, in a kind of composite, as well as on the surface of this silica.

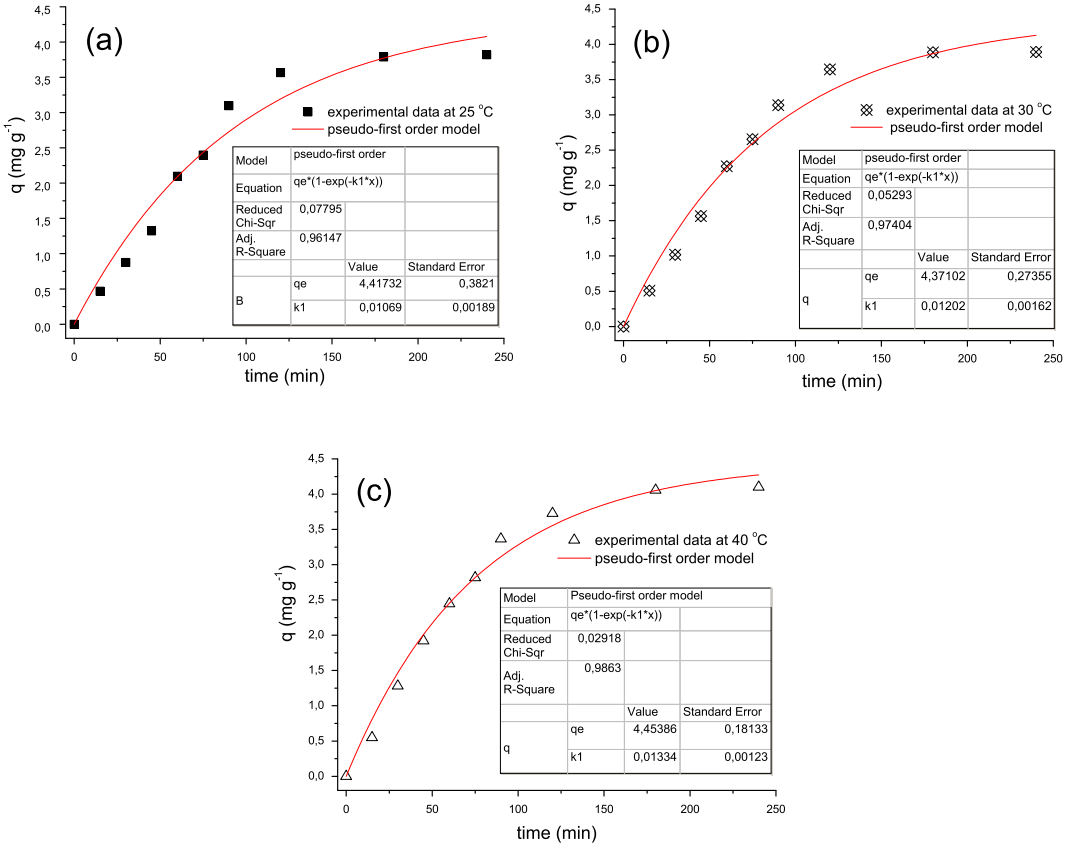

Figure 7. Kinetic data of q vs. time, and adjustments of the pseudo-first-order model to the data as a function of temperature: (a) 25 °C, (b) 30 °C and (c) 40 °C (duration of 4 h, N–NH_3 concentration of 50 mg L^{-1}, adsorbent concentration of 10 g L^{-1}, 170 rpm rotation speed, and pH 10).

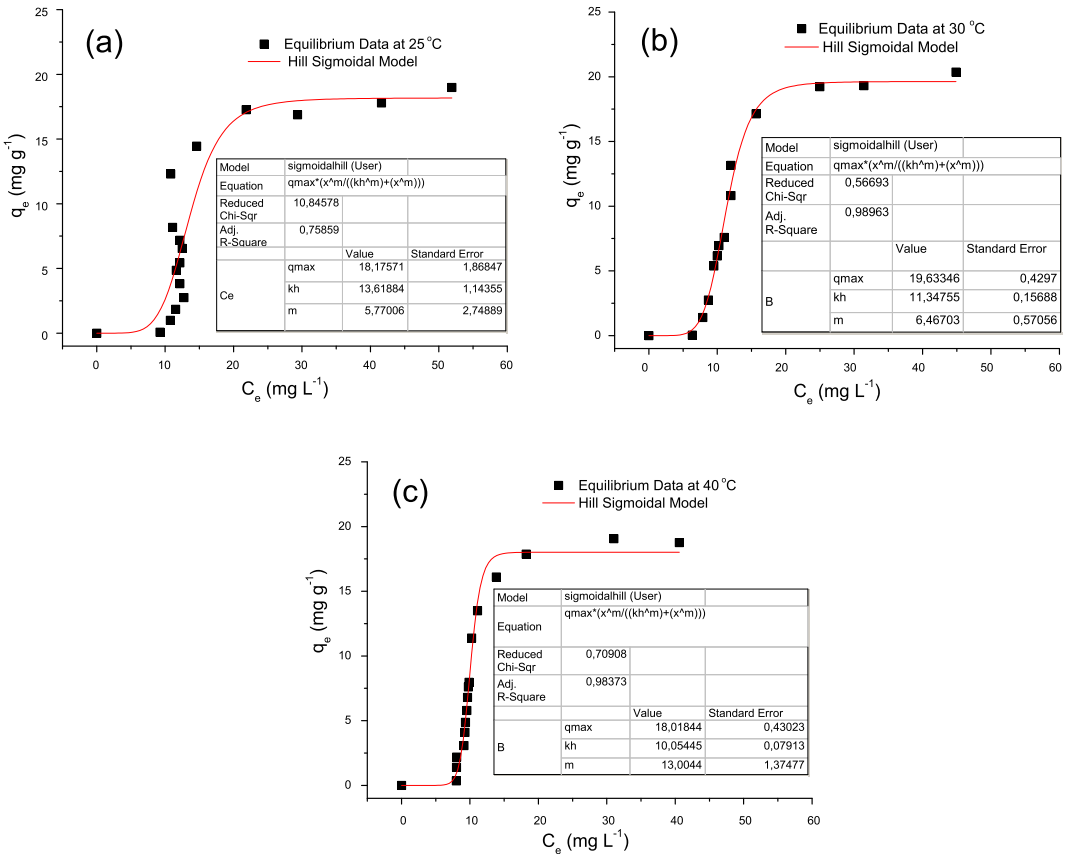

Figure 8. Equilibrium data q_e vs. C_e at temperatures of: (a) 25 °C, (b) 30 °C, and (c) 40 °C, at pH 10, 120 min duration, adsorbent concentration of 10 g L^{-1}, initial N–NH_3 concentrations of 10–250 mg L^{-1}, fitted to Hill's sigmoidal model.

Although the values determined through the texture analysis were not favorable for the use of compound (cri/H_3PO_4 1:3)$_2$ as an adsorbent, the test resulted in the removal of approximately 84% of ammonia nitrogen from aqueous solutions at pH 10, as mentioned earlier. Therefore, the study to determine the applicability of this material for the adsorption of N–NH_3 was performed as described below.

3.2. Kinetic tests

Figures 6 and 7 illustrate the N–NH_3 adsorption capacity of compound (cri/H_3PO_4 1:3)$_2$ as a function of pH and temperature, respectively.

The systems reached equilibrium between 120 and 150 min, and the best N–NH_3 adsorption was achieved at pH 10, with adsorption decreasing below or above this pH level. At pH levels below 10, the H^+ and NH_4^+ cations compete for the active sites in the adsorbent (Soltani et al., 2015). Conversely, at pH levels above 10, the molecular form of NH_3 predominates, reducing the number of ions to be adsorbed by the phosphate groups possibly contained in the adsorbent ($P_2O_7^{4-}$, PO_4^{3-}, HPO_4^{2-}, H_2PO^{4-}, etc.) (Ugurlu and Karaoglu, 2011; Zhang et al., 2011).

In Figure 7, which illustrates the adsorption process at different temperatures, note that the higher the temperature, the greater the adsorption capacity. The adsorption velocity constants of 0.011, 0.012 and 0.013 min^{-1} at 25, 30, 40 °C, respectively, were obtained by adjusting the data to the pseudo-first order model. This enabled us to apply a linear adjustment of ln k vs. 1/T using the Arrhenius equation, resulting in a pre-exponential factor of 0.32 ± 0.09 min^{-1} and an energy of 8329 ± 1696J mol^{-1}, indicating that the adsorption process occurs through physical interactions. The kinetic data did not fit the pseudo-second-order model satisfactorily.

3.3. Equilibrium assays

The adsorption isotherms shown in Figure 8 were created at temperatures of 25, 30, and 40 °C and at the most favorable pH, in order to analyze the mechanism of adsorption. As can be seen, the adsorption isotherms are type S2, which is typical of microporous adsorbents, presenting a sigmoidal shape that matches Hill's sigmoidal model (Giles et al., 1960).

This type of isotherm indicates that the adsorption process is governed by two mechanisms. The first is complexation, which is represented on the initial part of the concave curve and acts up to the inflection point (K_H), while the second mechanism is that of adsorption, which takes over starting at that point. In other words, the adsorption capacity of compound (cri/H_3PO_4 1:3)$_2$ on the monolayer is low up to the inflection point, but from there on the monolayer begins to cooperate with the subsequent layers, facilitating the adsorption process, following the slope of Hill's "S" curve (Limousin et al., 2007). The maximum adsorption capacity varies from 18.0 to 19.6 mg g^{-1} and the inflection point decreases slowly as the temperature increases, going from 13.6 mg L^{-1} at 25 °C to 10.0 mg L^{-1} at 40 °C, indicating that the increase in temperature contributes to the complexation step. Like the data of the kinetic tests, the equilibrium data did not fit Langmuir's sigmoidal model satisfactorily.

Complexation may give rise to the compound $MgNH_4PO_4$, whose composition is similar to that of the mineral struvite, of the same chemical formula. However, residual silica from chrysotile, which is also

present, may interact with ammonia nitrogen through its Brønsted acid sites (Ali et al., 2005). It is therefore difficult to determine the real nature of this complex. Moreover, low concentrations of N–NH_3 are used compared to the concentrations of adsorbent.

3.4. Recovery of the adsorbent

The XRD, DSC, and FTIR analyses of compound (cri/H_3PO_4 1:3)$_2$ recovered after two adsorption tests showed no significant change when compared to the initial material, indicating that the material retained its original structure. The TGA indicated a mass loss of 5.47%, which did not involve the solubilization of magnesium compounds since no Mg^{2+} ions were detected in the N–NH_3 solutions used in the adsorption tests. The adsorption test of the recovered material revealed an adsorption capacity of 19.0 mg g^{-1}, which is similar to that of the original material, thus confirming the reusability of the adsorbent.

The N–NH_3 adsorption capacity of the freshly prepared and recovered adsorbent was superior to that of some mineral adsorbents of ammonia nitrogen, such as lignite (3,4 mg g^{-1}) (Tu et al., 2019), clinoptilolite (8.1 mg g^{-1}) (Karadag et al., 2006) and kaolin (4.3 mg g^{-1}) (Zhu et al., 2012), however slightly lower than the modified activated sludge (32,7 mg g^{-1}) describeb by Yunnen et al. (2016).

3.5. Adsorption test on an effluent from a wastewater treatment plant

After the effluent came into contact with compound (cri/H_3PO_4 1:3)$_2$, the parameters under evaluation showed a noticeable decrease, indicating not only that the ammonia nitrogen concentration was reduced but also that contact with the adsorbent resulted in an improvement of all the parameters. A removal rate of 85.2% of the initial N–NH_3 concentration of 48.9 mg L^{-1} was achieved, which is similar to that achieved (84.6%) in the treatment of a synthetic solution containing a similar initial concentration of N–NH_3. The COD decreased by 24.6%, resulting in a final concentration of 99.7 mg of O_2 L^{-1}. The pH level of the raw wastewater, which was initially 7.5, was adjusted to 10.0, and after the wastewater was treated with compound (cri/H_3PO_4 1:3)$_2$, its pH level remained at 8.5. Furthermore, the color and turbidity levels of the effluent decreased by 46.7% and 50.4%, respectively.

The decrease in COD, color and turbidity parameters are related to the action of the adsorbent since the concentration of Ca^{2+} (6.6 ± 3.6 mg L^{-1}), Mg^{2+} (1.1 ± 0.8 mg L^{-1}), and Fe^{2+} (1.0 ± 0.8 mg L^{-1}) in the effluent is relatively low. These ions, precipitates at pH 10, and when in large amount, can offer a significative new interface for the adsorption of the species that eventually contribute to color, turbidity and COD.

4. Conclusions

The reaction of chrysotile and phosphoric acid heat-treated at 150 °C for 6 h resulted in the formation of a composite of amorphous silica with crystalline magnesium pyrophosphate. This material proved to be a suitable adsorbent to remove ammonia nitrogen in aqueous solutions with pH 10, presenting a removal rate of approximately 85% at 30 °C. The kinetic tests indicated that adsorption occurs through physical interactions with an activation energy of 8329 J mol^{-1}, fitting the experimental data to a pseudo-first-order mechanism. The equilibrium assays resulted in type S2 isotherms, indicating that the process of N–NH_3 removal begins with complexation, which occurs up to the inflection point, followed by adsorption. The resulting solid compound proved to be reusable, maintaining its original adsorption capacity when reused, without mass loss through solubilization. The material was applied to a real sample of effluent from a WTP, providing a very similar N–NH_3 removal rate to that achieved in the assays with N–NH_3 solutions. Compound (cri/H_3PO_4 1:3)$_2$ is therefore a feasible alternative for the removal of ammonia nitrogen from real effluents, and the treatment of chrysotile with H_3PO_4 also offers an alternative for the use of this mineral.

Declarations

Author contribution statement

Camila P. Girotto: Performed the experiments; Analyzed and interpreted the data; Wrote the paper.

Sílvia D. de Campos: Conceived and designed the experiments; Contributed reagents, materials, analysis tools or data.

Élvio A. de Campos: Conceived and designed the experiments; Analyzed and interpreted the data; Contributed reagents, materials, analysis tools or data; Wrote the paper.

Funding statement

This research did not receive any specific grant from funding agencies in the public, commercial, or not-for-profit sectors.

Competing interest statement

The authors declare no conflict of interest.

Additional information

No additional information is available for this paper.

References

Ali, M.I., Schneider, P.A., Hudson, N., 2005. Thermodynamics and solution chemistry of struvite. J. Indian Inst. Sci. 85, 141–149.

Anbalagan, G., Sivakumar, G., Prabakaran, A.R., Gunasekaran, S., 2010. Spectroscopic characterization of natural chrysotile. Vib. Spectrosc. 52, 22–127.

APHA, 2005. Standard Methods for the Examination of Water and Wastewater, 21st ed. American Public Health Association, Washington, DC.

Aramendía, M.A., Borau, V., Jiménez, C., Marinas, J.M., Romero, F.J., Ruiz, J.R., 1998. Characterization by XRD, DRIFT, and MAS NMR spectroscopies of a $Mg_2P_2O_7$ catalyst. J. Colloid Interface Sci. 202, 456–461.

Bernstein, D.M., Toth, B., Rogers, R.A., Sepulveda, R., Kinzendorf, P., Phillips, J.I., Ernst, H., 2018. Evaluation of the dose-response and fate in the lung and pleura of chrysotile-containing brake dust compared to chrysotile of crocidolite asbestos in a 28-day quantitative inhalation toxicology study. Toxicol. Appl. Pharmacol. 351, 74–92.

Celerier, H., Jouin, J., Mathivet, V., Tessier-Doyen, N., Rossignol, S., 2018. Composition and properties of phosphoric acid-based geopolymers. J. Non-Cryst. Solids 493, 94–98.

Espinoza-Quiñones, F.R., Módenes, A.N., Pauli, A.R., Palácio, S.M., 2015. Analysis of trace elements in groundwater using ICP-OES and TXRF techniques and its compliance with brazilian protection standards. Water Air Soil Pollut. 226. Art. 32.

Fogler, H.S., 2006. Elements of Chemical Reaction Engineering, 4th Edition. Prentice-Hall Inc., New Jersey.

Gilani, A.G., Najafgholizadeh, A., Khanghah, B.M., Gazani, M.N., 2018. Experimental and correlational study of phase equilibria in aqueous solutions of phosphoric acid with alcohols at different temperatures. J. Mol. Liq. 268, 553–560.

Giles, C.H., Macewan, T.H., Nakhwa, S.N., Smith, D., 1960. Studies in adsorption. Part XI. A system of classification of solution adsorption isotherms, and its use in diagnosis of adsorption mechanisms and in measurement of specific surface areas of solids. J. Chem. Soc. 3973–3993.

Ho, Y.S., Wase, D.A.J., Forster, C.F., 1996. Kinetic studies of competitive heavy metal adsorption by sphagnum moss peat. Environ. Technol. 17, 71–77.

Jastrzebski, W., Sitarz, M., Rokita, M., Bułat, K., 2011. Infrared spectroscopy of different phosphates structures. Spectrochim. Acta 79, 722–727.

Jiang, D.B., Yuan, S., Cai, X., Xiang, G., Zhang, Y.X., Pehkonen, S., Liu, X.Y., 2019. Magnetic nickel chrysotile nanotubes tethered with pH-sensitive poly (methacrylic acid) brushes for Cu(II) adsorption. J. Mol. Liq. 276, 611–623.

Karadag, D., Koc, Y., Turan, M., Armagan, B., 2006. Removal of ammonium ion from aqueous solution using natural Turkish clinoptilolite. J. Hazard Mater. 136, 604–609.

Khoualdia, B., Loungou, M., Elaloui, E., 2017. Adsorption of organic matter from industrial phosphoric acid (H_3PO_4) onto activated bentonite. Arab. J. Chem. 10, S1073–S1080.

Kusiorowskie, R., Zaremba, T., Piotrowski, J., Adamek, J., 2012. Thermal decomposition of different types of asbestos. J. Therm. Anal. Calorim. 109, 693–704.

Lagergren, S., 1898. On the theory of so-called adsorption dissolved substances. K. Sven. Vetenskapsakad. Handl. 24, 1–39.

Limousin, G., Gaudet, J.-P., Charlet, L., Szenknect, S., Barthès, V., Krimissa, M., 2007. Sorption isotherms: a review on physical bases, modeling and measurement. Appl. Geochem. 22, 249–275.

Liu, K., Feng, Q., Yang, Y., Zhang, G., 2007. Preparation and characterization of amorphous silica nanowires from natural chrysotile. J. Non-Cryst. Solids 353, 1534–1539.

Liu, K., Zhu, B., Feng, Q., Duan, T., 2013. Novel transparent and flexible nanocomposite film prepared from chrysotile nanofibers. Mater. Chem. Phys. 142, 412–419.
Maletaškić, J., Stanković, N., Daneu, N., Babić, B., SToiljković, M., Yoshida, K., Matović, B., 2017. Acid leaching of natural chrysotile asbestos to mesoporous silica fibers. Phys. Chem. Miner. 45, 343–351.
McCutcheon, J., Dipple, G.M., Wilson, S.A., Southam, G., 2015. Production of magnesium-rich solutions by acid leaching of chrysotile: a precursor to field-scale deployment microbially enabled carbonate mineral precipitation. Chem. Geol. 413, 119–131.
Mendelovici, E., Frost, R.L., Kloprogge, J.T., 2001. Modification of chrysotile surface by organosilanes: an IR photoacoustic spectroscopy study. J. Colloid Interface Sci. 238, 273–278.
Mousa, S., 2010. Study on synthesis of magnesium phosphate materials. Phosphorous Res. Bull. 24, 16–21.
Nakagaki, S., Castro, K.A.D.F., Machado, G.S., Halma, M., Drechsel, S.M., Wypych, F., 2006. Catalytic activity in oxidation reactions of anionic iron (III) porphyrins immobilized on raw and grafted chrysotile. J. Braz. Chem. Soc. 17, 1672–1678.
Petkowicz, D.I., Rigo, R.T., Radtke, C., Pergher, S.B., Dos Santos, J.H.Z., 2008. Zeolite Na/A from Brazilian chrysotile and rice husk. Microporous Mesoporous Mater. 116, 548–554.
Ribas, M.C., Adebayo, M.A., Prola, L.D.T., Lima, E.C., Cataluña, R., Feris, L.A., Puchana-Rosero, M.J., Machado, F.M., Pavan, F.A., Calvete, T., 2014. Comparison of a homemade coco as hell activated carbon with commercial activated for the removal of reactive violet 5 dye from aqueous solutions. Chem. Eng. J. 248, 315–326.
Rinaudo, C., Gastaldi, D., Belluso, E., 2003. Characterization of chrysotile, antigorite and lizardite by FT-Raman spectroscopy. Can. Mineral. 41, 883–890.
Rozalen, M., Huertas, F.J., 2013. Comparative effect of chrysotile leaching in nitric, sulfuric and oxalic acids at room temperature. Chem. Geol. 352, 134–142.
Salinas, E.L., Antonio, J.A.T., Manríquez, M.E., Cantú, M.S., Ramos, I.C., Cortez, J.G.H., 2019. Synthesis and catalytic activity of chrysotile-type magnesium silicate nanotubes using various silicate sources. Microporous Mesoporous Mater. 274, 175–182.
Soltani, R.D.C., Safari, M., Rezaee, A., Godini, H., 2015. Application of a compound containing silica for removing ammonium in aqueous media. Environ. Prog. Sustain. 34, 105–111.
Sugiyama, S., Manabe, T., Ioka, D., Nakagawa, K., Sotowa, K.I., Shigemoto, N., 2009. Removal of aqueous ammonium from industrial wastewater with magnesium hydrogen phosphate. Phosphorus Res. Bull. 23, 15–19.
Teixeira, A.P.C., Santos, E.M., Vieira, A.F.P., Lago, R.M., 2013. Use of chrysotile to produce highly dispersed K-doped MgO catalyst for biodiesel synthesis. Chem. Eng. J. 232, 104–110.
Tu, Y., Feng, P., Ren, Y., Cao, Z., Wang, R., Xu, Z., 2019. Adsorption of ammonia nitrogen on lignite and its influence on coal Water Slurry preparation. Fuel 238, 34–43, 2019.
Ugurlu, M., Karaoglu, M.H., 2011. Adsorption of ammonium from an aqueous solution by fly ash and sepiolite: isotherm, kinetic and thermodynamic analysis. Microporous Mesoporous Mater. 139, 173–178.
Valouma, A., Verganelaki, A., Kalaitzaki, P.M., Gidarakos, E., 2016. Chrysotile asbestos detoxification with a combined treatment of oxalic acid and silicates producing amorphous silica and biomaterial. J. Hazard Mater. 305, 164–170.
Wang, X., Lin, S., Yano, E., Yu, I.T.S., Courtice, M., Lan, Y., Christiani, D.C., 2014. Exposure-specific lung cancer risks in Chinese chrysotile textile workers and mining workers. Lung Canc. 85, 119–124.
Wypych, F., Adad, L.B., Mattoso, N., Marangon, A.A.S., Schreiner, W.H., 2005. Synthesis and characterization of disordered layered silica obtained by selective leaching of octahedral sheets from chrysotile and phlogopite structures. J. Colloid Interface Sci. 283, 107–112.
Wypych, F., Schreiner, W.H., Richard Jr., E., 2004. Grafting of phenylarsonic and 2-nitrophenol-4-arsonic acid onto disordered silica obtained by selective leaching of brucite-like sheet from chrysotile structure. J. Colloid Interface Sci. 276, 167–173.
Yunnen, C., Changshi, X., Nie Jinxia, N., 2016. Removal of ammonia nitrogen from wastewater using modified activated sludge. Pol. J. Environ. Stud. 25, 419–425.
Zaremba, T., Krzakala, A., Piotrowski, J., Garczorz, D., 2010. Study on the thermal decomposition of chrysotile asbestos. J. Therm. Anal. Calorim. 101, 479–485.
Zhang, M., Zhang, H., Xu, D., Han, L., Niu, D., Tian, B., 2011. Removal of ammonium from aqueous solutions using zeolite synthesized from fly ash by a fusion method. Desalination 271, 111–121.
Zhu, L., Ding, W., Feng, L., Dai, X., Xu, X., 2012. Characteristics of an aerobic denitrifier that utilizes ammonium and nitrate simultaneously under the oligotrophic niche. Environ. Sci. Pollut. Res. 19, 3185–3191.